Journal of Zhejiang University-SCIENCE A (Applied Physics & Engineering) in press
www.jzus.zju.edu.cn; www.springer.com/journal/11582
E-mail: jzus_a@zju.edu.cn

Research Article

https://doi.org/10.1631/jzus.A2300516

Permeability of structured porous media: numerical simulations and microfluidic models

Shaokai NIE[1,2,3], Pengfei LIU[1,2,3], Kexin CHEN[1,2,3], Wenyuan WANG[1,2,3], Yunmin CHEN[1,2,3], Bate BATE[1,2,3]✉

[1]*Institute of Geotechnical Engineering, College of Civil Engineering and Architecture, Zhejiang University, Hangzhou 310058, China*
[2]*Hypergravity Research Center, College of Civil Engineering and Architecture, Zhejiang University, Hangzhou 310058, China*
[3]*MOE Key Laboratory of Soft Soils and Geoenvironmental Engineering, Zhejiang University, Hangzhou 310058, China*

Abstract: In this study, permeability of structured porous media with microfluidic model is experimentally and numerically determined, and compared with the classic Kozeny-Carman (KC) equation. The Reynolds number (Re) varies from 0.83 to 142.98. It is observed that the threshold of the Reynolds number is 1. When Re is below the threshold, the permeability is independent of the Reynolds number. When Re is over this threshold, the viscous force plays a dominant role and the permeability decreases with the Reynolds number increment. The permeability also rises with the diameter increment. With the same micropillar diameter, the microfluidic model with triangular pillar arrangement yields 4.5%~7.4% lower permeability than that with square pillar arrangement. The tortuosity obtained by numerical simulation in the triangular-arrangement model is 5.1%~7.9% higher than that in the square-arrangement model. Based on the arrangement of micropillars, a tortuosity model is proposed for quasi-two dimensional microfluidic models. There is an inverse relationship between permeability and tortuosity. In addition, permeability generated by numerical simulation is consistent with that obtained experimentally. However, permeability estimated by the classic KC equation roughly agrees with experimental results when the porosity is between 0.50 and 0.60. A model proposed in this study is suitable for predicting the permeability of microfluidic models. Furthermore, anisotropy induced by the tilt angle (0°~90°) of a model rectangular micropillar arrangement causes preferential flow and decreases the effective porosity. When the tilt angle increases from 0° to 90°, the tortuosity declines from 2.04 to 1.03, causing the permeability to rise from 1.0×10^{-11} m^2 to 4.3×10^{-11} m^2.

Key words: Permeability; Microfluidic model; Porosity; Tortuosity; Anisotropy

1 Introduction

In recent years, porous media characterization has engendered a great deal of interest, due to issues associated with gas and oil production in shale and hydrate (Lefebvre *et al*. 2008; Cai *et al*., 2012; Kawagoe *et al*., 2016; De *et al*., 2018), as well as applications in chemical engineering (Rickenbach *et al.* 2014), fuel cells (Kumar and Reddy, 2003; Tawfik *et al*., 2007; Yang *et al*., 2017), microelectronics cooling (Lu *et al*., 1998), and biomedicine (Zhang, 2011). The most significant properties of porous media that affect the permeability and fluid transport phenomena, are porosity, pore interconnectivity, pore radius, tortuosity and specific surface area (Carman, 1939; Cai *et al*., 2012; Straughan and Harfash, 2013). It is important to understand the effect of these properties on the characteristics of fluid flow through porous media.

One of the most commonly measured properties, permeability, characterizes the difficulty of flow through porous media, and represents the pore interconnectivity for fluid conductivity (Collins, 1961). Measurement methods include indirect prediction and image analysis from experiments (Lock *et al*., 2002), as well as techniques involving nuclear magnetic resonance spectroscopy and scanning electron microscopy (Cardona and Santamarina, 2020). The Darcy law is known to be the most common experimental method for determining permeability:

$$-\frac{\mathrm{d}p}{\mathrm{d}x} = \frac{\mu}{K}U \tag{1}$$

where $\frac{\mathrm{d}p}{\mathrm{d}x}$ is the hydraulic gradient, μ is the dynamic viscosity of fluid, U is fluid superficial velocity, and

✉ Bate BATE, batebate@zju.edu.cn
Shaokai NIE, https://orcid.org/0000-0002-0887-0241
Bate BATE, https://orcid.org/0000-0002-8692-8402

Received Oct. 11, 2023; Revision accepted Feb. 22, 2024; Crosschecked

K is the intrinsic permeability of the porous medium. This relation is only applicable for viscous-dominated flows (Liu and Tran, 2018; Loosveldt *et al*., 2002). For $Re > 1$, the relationship becomes nonlinear and a modified Darcy equation called Forchheimer Law has been proposed (Lee and Yang, 1997):

$$-\frac{\mathrm{d}p}{\mathrm{d}x} = \frac{\mu}{K}U + \delta\rho U^2 \tag{2}$$

where δ is the inertial resistance coefficient related to the pore shape, pore size and porosity. This is also known as the non-Darcy coefficient.

The major fields of connected to microfluidics are: molecular analysis, biodefence, molecular biology, and microelectronics (Tamayol *et al*., 2011a). With advances in microfluidics and microfabrication techniques, flow through microfluidic model in describing the porous media has become an area of great interest (Wan and Wilson, 1994; Bazylak *et al*. 2008), such as flow rate and interface wettability impacts on immiscible displacement (Conn *et al*., 2014; Hu *et al*., 2018; Chen *et al*., 2023), fines migration and pore clogging (Pozrikidis, 1994; Auset and Keller, 2004; Yang *et al*., 2019; Cao *et al*., 2019; Yang *et al*., 2020a; Yang *et al*., 2020b; Yin *et al*., 2023), as shown in Fig. 1. There is no doubt that using a microfluidic model to study permeability of porous media shows great potential. Therefore, many papers have reported estimation of permeability using creeping flow of liquids in microchannels with integrated micropillars. The micropillars provide the solid structure in a microfluidic model, which represents the soil skeleton (formation matrix). The diameter of integrated micropillars usually ranges from 20 μm to 450 μm (Gunda *et al*., 2013; Tamayol *et al*., 2011b; Tamayol *et al*., 2012; Liu and Tran, 2018). Gunda *et al*. (2013) investigated single phase fluid flow through microchannels with integrated micropillars to calculate the pressure drop and flow resistance. The microchannels contained micropillars arranged in square and staggered formations. Chen (2021) also studied the permeability of a microfluidic model with seepage experiments. Chips with micropillars in a triangular arrangement showed higher pressure drops than those with micropillars in a square arrangement.

Numerical simulation plays an important role in the study of the porous media seepage mechanism at the micrometer scale. There are several numerical methods, such as the Computational Fluid Dynamics (CFD) (Tamayol *et al*., 2011c; Tamayol *et al*., 2012; Huang *et al*., 2020), the Lattice Boltzmann Method (LBM) (Zhou *et al*., 2022), and the Pore Network Model (PNM) (Raeesi and Piri, 2009). Tamayol *et al*. (2012) fabricated several microfluidic samples to investigate the accuracy of a theoretical model compared with experimental and numerical data. Microfluidic samples were fabricated with porosities in the range of 0.35 to 0.95, fiber diameters varying from 50 to 400 μm, and a channel depth of approximately 100 μm. Huang *et al*. (2020) developed a numerical model of laminar flow in porous media, with square particles. The Reynolds number, streamline, porosity, tortuosity, and fractal dimension were evaluated. Compared to other numerical methods, though the CFD method requires higher computational resources, it has fewer model parameters and does not require calibration.

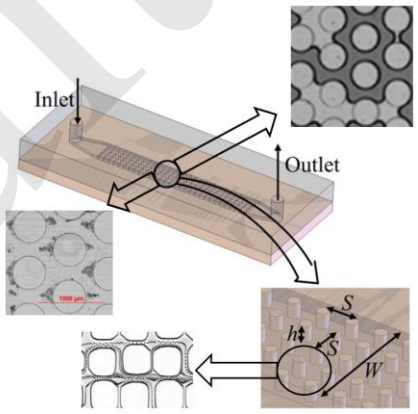

Fig. 1 A schematic illustration of a microfluidic model and its application for permeability, fines migration and multiphase displacement (Auset and Keller, 2004; Tamayol *et al*., 2012; Bate *et al*., 2022; Chen *et al*., 2023)

However, studies of permeability that are relevant to geotechnical engineering community and are carried out at microscale level with a microfluidic model in porous structures are limited. For example, there are deviations when measuring microchannel flow pressure drop to estimate the permeability of porous media, due to pressure loss at the inlet and outlet ports of the microchannel (Akbari *et al*., 2009; Nie *et al*., 2023). The flow condition in a microfluidic model seems to be limited to Darcy flow or creeping flow with low Reynolds numbers (Gunda *et al*., 2013; Tamayol *et al*., 2012). The wall effect is non-uniform variation of porosity near the wall in porous media,

and is neglected in low Reynolds number (Carlos *et al*., 2008, Chen *et al*., 2021). Moreover, it has been shown that the pressure drop obtained at the micro scale cannot be predicted adequately by large-scale correlations (Kosar *et al*., 2005; Yazdchi et al., 2011). The existing theoretical models fail to predict the permeability of microfluidic model accurately (Gunda *et al*., 2013; Serrenho and Miguel, 2009; Wagner, *et al*., 2021). Few studies have investigated the influence of microchannels with large particle diameters and moderate Reynolds number on the permeability of microfluidic models.

The goal of this study was to assess complementary fluid-flow to estimate the permeability of microfluidic models. These particular models had square or staggered arrangements of circular or rectangular micropillars when the experimental Reynolds number varied between 0.83-142.98. The effect of Reynolds number, anisotropy, tortuosity and porosity, on permeability are discussed. We also discuss the effect of microchannel depth on permeability. In addition, an analytical tortuosity model based on the 2D rectangular and circular micropillar is proposed, respectively. The experimental results are compared with those obtained by numerical simulation and the prediction model proposed in this study. We investigated the applicability of the Kozeny-Carman equation for the microfluidic model, and analyzed the fluid flow streamline in the model via a microscale particle-image velocimetry (μPIV) experiment.

2 Theoretical background

2.1 Reynolds number for microfluidic model flow

Dybbs and Edwards (1984) studied the microscopic fluid dynamics of dye fluid flowing through hexagonally packed spheres, and proposed Reynolds number:

$$Re = \frac{\rho U D_{\mathrm{h}}}{\mu} \tag{3}$$

where ρ is the fluid density, U is the average pore velocity, and D_{h} is the average characteristic length scale for the pores. For obstacles like fibers or particles, D_{h} can be re-written as:

$$D_{\mathrm{h}} = \frac{4\varepsilon}{(1-\varepsilon)a_{\mathrm{v}}} \tag{4}$$

where $a_{\mathrm{v}} = \frac{6}{d}$, d is the particle diameter. The experimental Reynolds numbers here varied between 0.83-142.98.

Four flow regimes are defined based on this Reynolds number (Dybbs and Edwards, 1984): (1) $Re < 1$, creeping-flow regime; (2) $1 - 10 < Re < 150$, inertial-flow regime; (3) $150 < Re < 300$, unsteady laminar-flow regime; and (4) $300 < Re$, unsteady- and chaotic-flow regime.

2.2 Kozeny-Carman equation and tortuosity

The well-known empirical approach for predicting the permeability of porous media is expressed by the Kozeny-Carman equation (Carman, 1956):

$$K = k\left(\frac{\mu}{\gamma_{\mathrm{p}}}\right) = \frac{1}{CS^2}\frac{\varepsilon^3}{(1-\varepsilon)^2} = \frac{1}{C_0\tau^2 S^2}\frac{\varepsilon^3}{(1-\varepsilon)^2} \tag{5}$$

where K is the intrinsic permeability (m^2), k is the permeability coefficient ($\mathrm{m/s}$), γ_{p} is the fluid bulk density, C is the Kozeny-Carman constant, S is the specific surface area and ε is the porosity. The value of C depends on factors including the tortuosity τ and the shape of grains C_0 (Wagner *et al*., 2021). τ is defined as follows (Carman, 1956):

$$\tau = \frac{L_{\mathrm{e}}}{L} \tag{6}$$

where L_{e} is the length of the streamlines and L is the sample length.

Tortuosity is related to the pore size, particle shape and porosity of porous media, in addition to other factors. Various empirical expressions are presented in Table 1 to describe this. Tortuosity models have been obtained by considering particle size and shape (Comiti and Renaud, 1989; Koponen *et al*., 1996; Wang, 2014), 2D particle arrangement (Yu and Li 2004; Lanfrey *et al*., 2010), and the topological properties of Sierpinski carpet (Selly, 2013; Khabbazi and Bazylak, 2015). However, the unified conclusion to obtain tortuosity value remains unknown, especially for the effect of particle arrangement on tortuosity.

In this study, we obtained tortuosity by numerical simulation (CFD). The length of streamlines in the characteristic plane is calculated by accumulating the coordinate distance of each fluid particle based on

Eq. (6), as shown in Fig. 2. The characteristic plane is defined as the middle height plane of the microfluidic model. That is, $h_1 = 0.025$ μm, because the height of the microfluidic model used in this study was 0.05 μm. It visually indicated that streamline patterns from numerical simulation corresponded to the experimental measurements provided in Appendix A.

$$l_1 = \sum_i \sqrt{(x_i - x_{i-1})^2 + (y_i - y_{i-1})^2} \quad (7)$$

$$\tau = \sum_1^i \frac{l_i}{iL} \quad (8)$$

where l_1 is one streamline, and x_i and y_i are the coordinates of fluid particles.

Table 1 Expressions of tortuosity τ

Authors	Equation	Notes
Comiti and Renaud (1989)	$\tau = 1 - P\ln(\varepsilon)$	P is a fitting coefficient and is 0.63 for cubic particles and 0.41 for spherical particles
Koponen et al. (1996)	$\tau = 1 + 0.8(1-\varepsilon)$	Fluid flowed through freely arranged square particles
Yu and Li (2004)	$\tau = \frac{1}{2}[1 + \frac{1}{2}\sqrt{1-\varepsilon} + \sqrt{1-\varepsilon}\frac{\sqrt{(\frac{1}{\sqrt{1-\varepsilon}} - 1)^2 + \frac{1}{4}}}{1-\sqrt{1-\varepsilon}}]$	Assuming two-dimensional square particles in an equilateral-triangle arrangement
Selly (2013)	$\tau = -0.7145\varepsilon + 1.6571$	Proposing a two-dimensional fractal model of porous substance constructed by Randomized Sierspinski Carpets
Wang (2014)	$\tau = -0.42\varepsilon + 1.35$	Simulating the fluid flow in intervals of dense spheres by LBM
Khabbazi and Bazylak (2015)	$\tau = \left(1 - \frac{4}{\pi}\right)\varepsilon + \frac{4}{\pi}$	Relationship between tortuosity and porosity within fractal geometries of Sierpinski carpet
Zhang et al. (2020)	$\tau = \frac{3}{8}\left\{\sqrt{\left[1-\sqrt{(1-\varepsilon)m}\right]^2 + tan^2\left[(1-\varepsilon)^{\frac{1}{3}}\theta\right]} + \sqrt{\frac{tan^2[(1-\varepsilon)^{1/3}\theta]}{\left[1-\sqrt{(1-\varepsilon)m}\right]^2}}\right\} + \frac{2-\sqrt{(1-\varepsilon)m}}{8cos[(1-\varepsilon)^{1/3}\theta]} + \frac{\sqrt{(1-\varepsilon)m}}{8[1-\sqrt{(1-\varepsilon)m}]} + \frac{5}{8}\sqrt{(1-\varepsilon)m}$	A mathematical model for two-dimensional square solid particles with m as the anisotropic parameter and θ as the retarding parameter

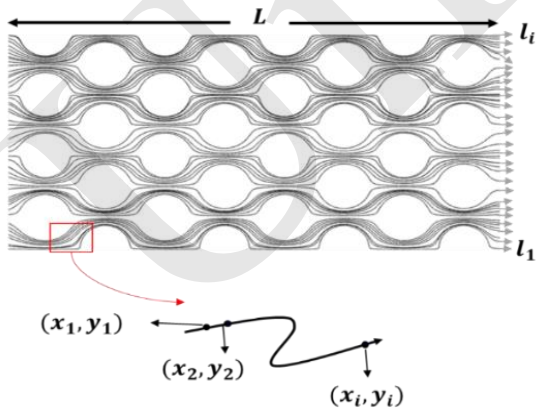

Figure 2. Schematic diagram of streamline for microfluidic models

3 Materials and Experimental Methods

3.1 Materials

Deionized (DI) water was used as the liquid phase. Monodisperse fluorescent microspheres (Polystyrene microspheres) with a density and diameter of 1.05 g/cm^3 and 1.0 μm, respectively, were purchased to serve as the tracer particles. They were used to visualize the fluid streamline, which had reliable flow behavior when the diameter of fluorescent microspheres was less than 1.0 μm under laminar flow (Shen and Chen, 1989).

3.2 Experimental apparatus

The experimental system of fluorescent microscopy combined with a microfluidic chip is presented in Fig. 3. Water was injected with a syringe pump (Harvard PHD ULTAR). The controllable injection rate ranged from 0.1 μL/min to 5 L/min and the injection pressure of DI water was measured with

pressure sensors (uProcess Analog Sensor Manifold 4AM01, USA). We used the fluorescence microscopy method to collect image for fluid-streamline and velocity detection. All images were captured with a reverse microscope (Nikon Inverted Research Microscope ECLISE Ti2-U). Data were acquired through the Cellsens software provided by Nikon.

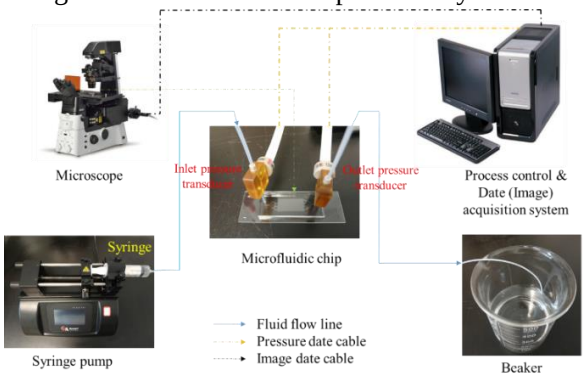

Figure 3. Schematic of the experimental system used for pressure drop measurement.

The hydrophilic borosilicate glass microchannels, consisting of micropillars, were fabricated using the deep reactive ion etching (DRIE) microfabrication technique. A schematic of the entire microfluidic chip is shown in Fig. 4a. Microchannels with dimensions of 1 cm (width) × 2 cm (length) × 50 μm (depth) were built into the microfluidic chip, which consisted of uniform micropillars. Branch inlet and outlet regions with a dimension of 800 μm (width) × 50 μm (depth) were connected to the microchannels. The length of branch inlet or outlet regions is illustrated in Fig. 4b. For circular micropillars (Fig.4c), we investigated square and triangular arrangements of microchannels with micropillar diameters of 500, 1000 and 2000 μm, and porosities of 0.54 and 0.60 (Table 2). The height for the square arrangement of microchannels with a micropillar diameter of 500 μm and porosity of 0.60 ranged from 30 μm to 200 μm. The porosity for the square microchannel arrangement with a diameter of 500 μm and microchannel height of 50 μm ranged from 0.33 to 0.90.

Table 2. Geometrical dimensions of different microfluidic models considered in the present work

Type of microfluidic model	Micropillar shape	Micropillar arrangement	Micropillar dimensions		Porosity	Tilt angle
			D/a_1 (μm)	S_0/b_1 (μm)	ε	θ
Asq-0.60-500	circular	square	500	707	0.60	\
Asq-0.60-1000	circular	square	1000	1414	0.60	\
Asq-0.60-2000	circular	square	2000	2828	0.60	\
Ast-0.60-500	circular	triangular	500	758.5	0.60	\
Ast-0.60-1000	circular	triangular	1000	1519	0.60	\
Ast-0.60-2000	circular	triangular	2000	2631	0.60	\
Ast-0.54-500	circular	triangular	500	707.1	0.54	\
Ast-0.54-1000	circular	triangular	1000	1414	0.54	\
Ast-0.54-2000	circular	triangular	2000	2828.4	0.54	\
Asq-0.41-0^o	rectangular	square	1600	400	0.41	0^o
Asq-0.41-30^o	rectangular	square	1600	400	0.41	30^o
Asq-0.41-45^o	rectangular	square	1600	400	0.41	45^o
Asq-0.41-60^o	rectangular	square	1600	400	0.41	60^o
Asq-0.41-90^o	rectangular	square	1600	400	0.41	90^o
Ast-0.41-0^o	rectangular	triangular	1600	400	0.41	0^o
Ast-0.41-30^o	rectangular	triangular	1600	400	0.41	30^o
Ast-0.41-45^o	rectangular	triangular	1600	400	0.41	45^o
Ast-0.41-60^o	rectangular	triangular	1600	400	0.41	60^o
Ast-0.41-90^o	rectangular	triangular	1600	400	0.41	90^o

Notes: D is micropillar diameter, S_0 is the distance between two neighboring micropillars, a is the length of a rectangular micropillar, b is the width of a rectangular micropillar, Asq indicates square arrangement and Ast indicates triangular arrangement. For example, Asq-0.60-500 refers to a circular micropillar with square arrangement, in which the micropillar diameter is 500 μm, and the porosity is 0.60. Asq-0.41-0^o refers to a rectangular micropillar with square arrangement in which the porosity is 0.41 and the tilt angle is 0^o.

Soils are composed of mineral grains. Grain size distribution and particle shape both play a critical role in soil macroscale behavior. Inherent fabric in non-spherical coarse-grained soils always posited to a rectangular flaky particle for conceptual model, especially for undrained strength anisotropy (Santamarina and Cho, 2004). Here, we propose a facile microfluidic model to explore the effect of anisotropy on permeability (Fig. 4d). The rectangular micropillar model can also be used to simulate two-dimensional fractured rock mass flow. For rectangular micropillars (Fig.4d), the intrinsic porosity was 0.41. The unit cell size was 400 μm (b_1) × 1600 μm (a_1) (width × length) and the size of the pore throat was 200 μm. The tilt angle for both triangular and square arrangements was between 0° and 90°.

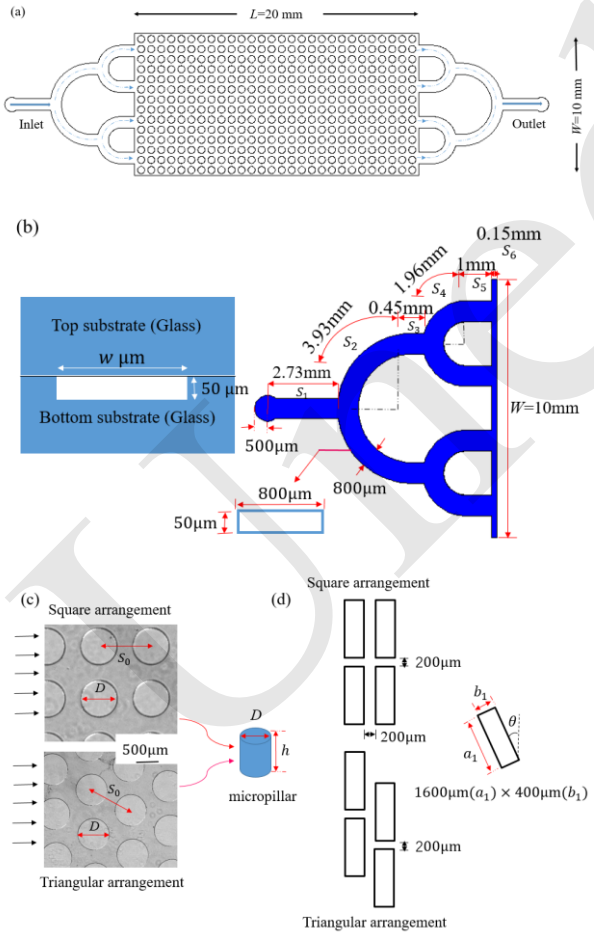

Figure 4. (a) Schematic diagram of the microfluidic chip; (b) Close-up view of the inlet port channels; (c) Dimensions of circular micropillars; (d) Dimensions of rectangular micropillars

3.3 Calibration of pressure drop in the microfluidic model

DI water was injected into the microchannels with the syringe pump at appropriate flow rates. No leakage was observed, and the flow was stable. We obtained the total pressure drop by subtracting outlet pressure from inlet pressure. The composition of measured pressure drop was given by Akbari *et al.* (2009):

$$\Delta P_{\mathrm{F}} = \Delta P_{\mathrm{M}} - (\Delta P_{\mathrm{t}} + \Delta P_{\mathrm{c}} + \Delta P_{\mathrm{N}} + \Delta P_{\mathrm{D}} + \Delta P_{\mathrm{x}} + 2\Delta P_{\mathrm{b}} + \Delta P_{\mathrm{v}}) \quad (9)$$

where ΔP_{F} is the pressure drop in the fully developed region, ΔP_{t} is the pressure loss due to flow in the tubes connecting the transducer to the microchannel inlet, ΔP_{c} is the pressure loss due to flow in the inlet and outlet channels, ΔP_{N} and ΔP_{x} are the inlet and exit losses, ΔP_{b} is the pressure drop due to 90 deg bends, ΔP_{D} is the developing region loss, and ΔP_{v} is the pressure drop corresponding to the electro-viscous effect.

Bahrami *et al.* (2007) proposed a solution to determine the pressure drops in the inlet and outlet rectangular channels of a microfluidic chip. The laminar flow in microchannels is single-phase and fully developed. We observed that the Poiseuille number was only a function of geometrical parameters of the cross-section when the fluid properties and flow rates were constant. The proposed model is expressed as follows:

$$4f_{\mathrm{f}} = \frac{2\Delta P D_{\mathrm{h}}}{\rho u^2 L} \quad (10)$$

$$f_{\mathrm{f}} Re_{\sqrt{\mathrm{A}}} = \frac{12}{[1-\frac{192}{\pi^5}\epsilon\tanh\frac{\pi}{2\epsilon}](1+\epsilon)\sqrt{\epsilon}} \quad (11)$$

$$Re_{\sqrt{\mathrm{A}}} = \frac{\rho u\sqrt{A}}{\mu} \quad (12)$$

where f_{f} is the Fanning friction factor and $4f_{\mathrm{f}} = f$ (Yang *et al.*, 2019), $Re_{\sqrt{\mathrm{A}}}$ is the Reynolds number defined based on the square root of area, $\sqrt{A}$. $\epsilon = \frac{c}{b}$ is the aspect ratio because b and c are the major and minor semi-axes of the cross-section, $b \geq c$. $\sqrt{A}$ (as the characteristic length scale for non-circular channels), is a more appropriate length scale since it is found through analysis (Yovanovich, 1974).

ΔP_{t} and ΔP_{v} were neglected. ΔP_{c} was calcu-

lated based on the diameter and length of connecting tubes. ΔP_D and ΔP_v were lower than 0.3% compared to the measured pressure drop. ΔP_N, ΔP_x, and ΔP_b were lower than 1% compared to the measured pressure drop with a small Reynolds number, and lower than 5% with a larger Reynolds number (Akbari *et al*., 2009).

3.4 Numerical simulations

3.4.1 Physical model

Based on the experimental microfluidic chips, the dimensions of the numerical physical model are shown in Fig. 5. Upper and lower boundaries were fixed and flow direction was from left to right. DI water was used as the fluid phase and its density and viscosity were 998.2 $\mathrm{kg/m^3}$ and 0.001 $\mathrm{kg/m \cdot s}$, respectively.

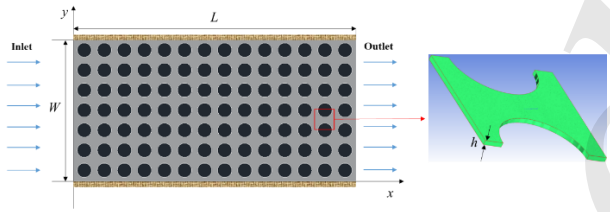

Figure 5. Diagram of numerical physical model. The model's length $L = 20$ mm, inner width $W = 10$ mm and channel depth $h = 50$ μm. The black circles are micropillars and the grey region is the pore channels

3.4.2 Governing equations

When the Reynolds number is small, the following assumptions are made to simplify calculation of the numerical solution: 1) The liquid-solid interface is set to the no-slip boundary. 2) There is steady laminar flow in the microchannels. 3) The mass force item can be disregarded. 4) The physical parameters of the fluid are constant.

Then, the continuity equation for incompressible Newtonian fluid is set to be the governing equation:

$$\frac{\partial u_x}{\partial x} + \frac{\partial u_y}{\partial y} + \frac{\partial u_z}{\partial z} = 0 \quad (13)$$

The momentum equations are:

$$u_x \frac{\partial u_x}{\partial x} + u_y \frac{\partial u_x}{\partial y} + u_z \frac{\partial u_x}{\partial z} = -\frac{1}{\rho}\frac{\partial p}{\partial x} + \mu\left(\frac{\partial^2 u_x}{\partial x^2} + \frac{\partial^2 u_x}{\partial y^2} + \frac{\partial^2 u_x}{\partial z^2}\right) \quad (14)$$

$$u_x \frac{\partial u_y}{\partial x} + u_y \frac{\partial u_y}{\partial y} + u_z \frac{\partial u_y}{\partial z} = -\frac{1}{\rho}\frac{\partial p}{\partial y} + \mu\left(\frac{\partial^2 u_y}{\partial x^2} + \frac{\partial^2 u_y}{\partial y^2} + \frac{\partial^2 u_y}{\partial z^2}\right) \quad (15)$$

$$u_x \frac{\partial u_z}{\partial x} + u_y \frac{\partial u_z}{\partial y} + u_z \frac{\partial u_z}{\partial z} = -\frac{1}{\rho}\frac{\partial p}{\partial z} + \mu\left(\frac{\partial^2 u_z}{\partial x^2} + \frac{\partial^2 u_z}{\partial y^2} + \frac{\partial^2 u_z}{\partial z^2}\right) \quad (16)$$

where u_x, u_y and u_z are the water velocity, p is the pressure, ρ is the density, and μ is the kinematic viscosity of water.

3.4.3 Boundary conditions

The inlet boundary condition is given by:

$$x = 0,\ u_x = u_0,\ u_y = 0, u_z = 0 \quad (17)$$

The outlet boundary condition can be written as:

$$x = L,\ \frac{\partial u_x}{\partial x} = \frac{\partial u_y}{\partial x} = \frac{\partial u_z}{\partial x} = 0 \quad (18)$$

The liquid-solid interfaces are assumed to be no-slip boundaries. Therefore, velocity at these interfaces satisfies the following relationship:

$$u_x = u_y = u_z = 0 \quad (19)$$

3.4.4 Numerical approach

We used ANSYS FLUENT 2019 R3 (Canonsburg, Pennsylvania, USA), Computational Fluid Dynamics (CFD) program, to simulate the seepage in 3D. A structured grid system was used to divide the computational domain in our model. The liquid phases in the microchannel were divided into hexahedral elements and local mesh refinement was conducted for the microchannel region to improve calculation accuracy. Symmetry boundary conditions was applied at the sides of the unit cell under consideration. In order to ensure the reliability of numerical results, we conducted a grid independence test (see Fig. 6a). At a velocity of 3.3×10^{-4} m/s, the inlet pressure increased with more grid-node numbers. When the number of grid nodes was over 1.1×10^6, inlet pressure reached equilibrium. The maximum grid size was 0.02 mm.

We used the SIMPLEC algorithm to calculate

the pressure-velocity coupling. For better convergence accuracy of the calculation, we applied the Gauss–Seidel method, taking into consideration the over-relaxation factor. We adopted double precision, and discretized the momentum equation using a second-order upwind scheme. The relaxation factor was set to 0.5, and the residual between the two iteration steps was set to 10^{-6}. When the maximum residuals of velocity were 10^{-6}, the iteration was regarded as convergent. A comparison between the numerical and experimental results for the inlet pressure of Asq-0.60-1000 is given in Fig. 6b. The maximum deviation between the numerical and experimental results was 5.6%. It was under control, and thus we considered the current model to be reasonable and able to predict the seepage characteristics of the microfluidic chip model.

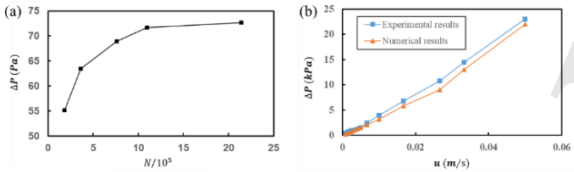

Figure 6. (a) Grid independence test; (b) Validation of numerical microfluidic chip model of Asq-0.60-1000

4 Results and Discussion

4.1 Effects of porosity on tortuosity

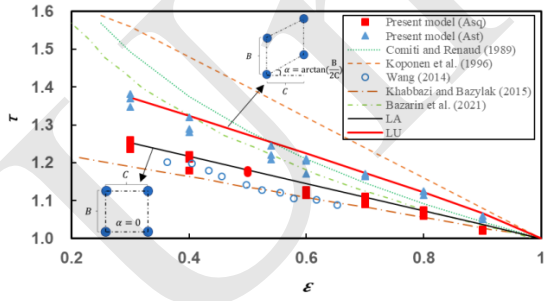

Figure 7. Comparison of tortuosity obtained by numerical simulations and models in the literature

Figure 7 presents a comparison of tortuosity generated by numerical simulations of square and triangular arrangements, and found for models in previous studies (with porosity ranging from 0.3 to 1.0). Generally, tortuosity appears to decrease as the porosity increase. The traditional assumption is that tortuosity is only dependent on porosity (Koponen et al., 1996; Wang, 2014; Khabbazi and Bazylak, 2015), but the 2D particle arrangement also has an effect on it. In our experiments, we found that with the same porosity, models with triangular arrangement always yielded higher tortuosity than those with square arrangement. For example, the tortuosity of Ast-0.60-500 was 1.21, higher than that of Asq-0.60-500 (1.13), which means that the flow path would be more tortuous with a triangular arrangement than with a square arrangement. This is evident in Fig. 7. On the other hand, as the porosity increased from 0.30 to 1.00, the tortuosity for the triangular arrangement decreased from 1.37 to 1.00, while it decreased from 1.26 to 1.00 for the square arrangement. The deviation between triangular and square arrangements with the same porosity decreased as porosity increased. This result indicated that the particle obstruction to the fluid weakened when the porosity increased from 0.30 to 1.00.

The relationship between tortuosity and porosity has been reported extensively, as shown in Table 2. Results obtained by Koponen *et al.* (1996) and Khabbazi and Bazylak (2015) showed that tortuosity decreases linearly when porosity increases. Yet, Comiti and Renaud (1996) and Bazarin *et al.* (2021) proposed a nonlinear relationship. In this study, models were postulated for two-dimensional uniform porous media and no-slip boundary conditions. Khabbazi and Bazylak (2015) obtained an analytical tortuosity-porosity correlation for a 2D circular-based Sierpinski carpet with square arrangement, which was consistent with our experimental results for the model with square arrangement. Meanwhile, the tortuosity of our experimental model with triangular arrangement was roughly similar to that of the model proposed by Bazarin *et al.* (2021), in which the fractal geometry a 2D Sierpinski carpet was solved by the lattice Boltzmann method. However, it is notable that when the porosity was larger than 0.7, the numerical tortuosity of our triangular arrangement models was higher than that obtained by Bazarin *et al.* (2021). The deviation may be due to the assumption in their study of fractal geometry of square particles, while uniform circular particles were used in this study. Furthermore, because of the different assumptions and boundary effects, such as particle size and shape (Comiti and Renaud, 1989; Koponen *et al.*, 1996; Wang, 2014), 2D vs. 3D random particle-arrangement simulation

(Bazarin *et al*., 2021), topological properties of Sierpinski carpet (Khabbazi and Bazylak, 2015), value deviations of tortuosity exists in all these tortuosity models, as shown in Fig. 7. However, they all presented the negative tendency between the tortuosity and porosity.

We propose a mathematical model for calculating 2D circular-based soil tortuosity for different particle arrangements:

$$\tau = \frac{1}{\cos\left[(1-\varepsilon)^{\frac{1}{3}}\alpha\right]} + \left(\frac{\pi}{4} - \frac{1}{2}\right)\frac{4(1-\varepsilon)}{\pi} \tag{20}$$

where α is the horizontal angle between two particles, which arranges from 0 to $\arctan(B/2C)$. As shown in Fig. 7, the special case when α equals 0 is defined as the line of lower-limit arrangement (LA), and the normal case when α equals $\arctan(B/2C)$ is defined as the line of upper-limit arrangement (LU). More details are shown in Appendix B.

4.2 Effects of porosity on tortuosity

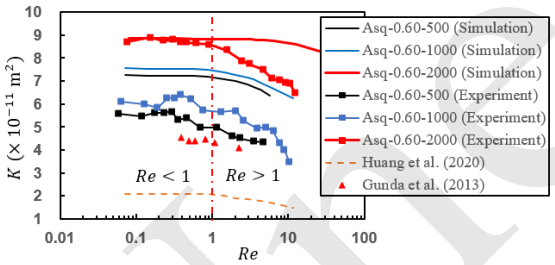

Figure 8. Effects of Reynolds number on permeability of square arrangement microfluidic chips with a porosity of 0.60

The relationship between the permeability and Reynolds number of sample Asq-0.60 is depicted in Fig. 8. Generally, microfluidic chips with larger micropillar diameter induced larger permeability compared to those with smaller micropillar diameter in both experiments and numerical simulations. The ratio of micropillar wetted surface area to channel side wall area ($L \times W$) for Asq-0.60-500, Asq-0.60-1000 and Asq-0.60-2000 was 15.39, 7.70 and 4.40, respectively. With grater micropillar diameter, unit micropillar wetted surface area decreased, causing the side friction to decrease in turn. Therefore, microfluidic chips with smaller micropillar diameter yielded lower permeability than those with larger micropillar diameter, with the same porosity.

As shown in Fig. 8, when the Reynolds number $Re < 1$, the permeability was almost independent of the Reynolds number, which was quite obvious in the numerical simulation results. Further increase in the Reynolds number led to lower permeability. Huang *et al*. (2020) developed a heterogeneous numerical model of laminar flow in 2D porous media. The correlation they found between permeability and Reynolds number was in line with the results mentioned above. The same conclusion was also obtained in microfluidics experiments done by Gunda *et al*. (2013). This was that Darcy law could not accurately describe the seepage characteristics of the porous media when $Re > 1$. When the Reynolds number is large, it was proved that the liquid flow in porous media is affected by both inertial and viscous forces, and the side friction increases (Antohe *et al*., 1997). Based on the Darcy-Forchheimer Law, Eq. (2) can be rewritten to the following expression:

$$-\frac{\mathrm{d}p}{U\mathrm{d}x} = \frac{\mu}{K} + \delta\rho U \tag{21}$$

We obtained the relationship diagram for $\frac{\Delta p}{UL}$ and U, which enabled us to calculate the permeability by the intercept. The inertial resistance coefficient δ (m^{-1}) was calculated by the slope, and was found to be 62456, 64689, and 82125 for Asq-0.60-500, Asq-0.60-1000, and Asq-0.60-2000, respectively.

The permeability obtained with our numerical simulations was 10% higher than that obtained in the experiments (Fig. 8). We proposed the following explanations for this discrepancy: 1) no-slip boundary conditions and smooth sides were applied in the numerical simulation, but side friction was included in the experiments; 2) the pressure drop caused by inlet and exit losses and the electro-viscous effect were neglected; 3) the hydraulic pressure measured by pressure sensors varied in the experiments.

4.3 Effects of micropillar arrangement on permeability

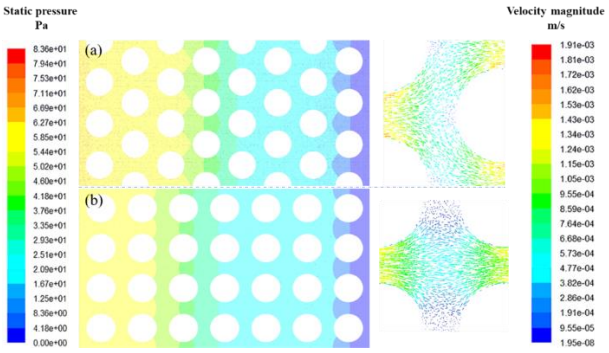

Figure 9. Effects of micropillar arrangement on pressure distribution and velocity vector distribution at a velocity of 0.00033 m/s: (a) Ast-0.60-2000; (b) Asq-0.60-2000.

Flow characteristics including pressure distribution and velocity vector distribution for models Ast-0.60-2000 and Asq-0.60-2000 at a velocity of 0.00033 m/s, are demonstrated in Fig. 9. With the same porosity, the triangular-arrangement model yielded a larger pressure drop (65 Pa) than the square arrangement model (57 Pa). The maximum pressure was in the inlet, and it decreased with the flow direction. The maximum velocity vector of the pore throat in the triangular-arrangement model was 1.78×10^{-3} m/s, higher than that in the square arrangement model (1.53×10^{-3} m/s). We observed that flow in the triangular-arrangement model was divided into two parts, causing the difficulty of flow seepage and increasing of flow path. However, the flow seeped mostly straight in the horizontal pore-channel direction in the square-arrangement model. The velocity vector in the vertical pore throat was nearly zero.

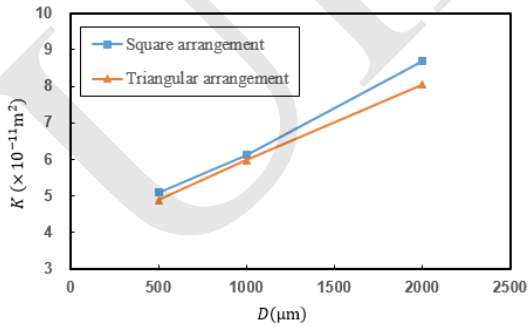

Figure 10. Comparison of experimental permeability with different micropillar arrangements and a porosity of 0.60

To further investigate the effect of micropillar arrangement on the permeability of microfluidic chips, we considered microchannels with square and triangular micropillar arrangement and a porosity of 0.60. A comparison of experimental permeability with different micropillar arrangements is presented in Fig. 10. With the same micropillar diameter, the triangular-arrangement model yielded lower permeability (4.5%~7.4%) than the square-arrangement model. This difference was more pronounced with larger micropillar diameter. When the porosity and micropillar diameter are the same, tortuosity is the only variable parameter based on the KC equation, which has an effect on the permeability of microfluidic chips. From Fig. 7, one can see that the tortuosity values in the triangular-arrangement model were 5.1%~7.9% higher than in the square-arrangement model, with a porosity of 0.60. This deviation led to a difference in permeability of the microfluidic models with different arrangements.

4.4 Effects of anisotropy on permeability

The effects of tilt angle on the tortuosity and velocity vector of the unit-cell model with rectangular micropillar arrangement are shown in Fig. 11a. With the same tilt angle, the tortuosity of the triangular-arrangement model was higher than that of the square-arrangement model. In the triangular-arrangement model, we observed that the larger the tilt angle, the lower the tortuosity and velocity in the micro-channel. The maximum tortuosity was 2.0397 when the tilt angle was 0°. When the tilt angle was 90°, the tortuosity was nearly 1.0, which was caused by the horizontal direction channel of preferential flow. The same tendency was also presented in the square-arrangement model, except for a tilt angle of 0°, at which the tortuosity was only 1.0389, far lower than the value (1.3918) when the tilt angle was 30°. In addition, when the tilt angle was 0°, the velocity vector of the square-arrangement model was almost in the horizontal flow direction channel and the velocity magnitude was as high as 5.95×10^{-3} m/s, which was higher than in other models. This can be explained by the fact that the flow rate was constant and the velocity was in reverse proportion to the flow area.

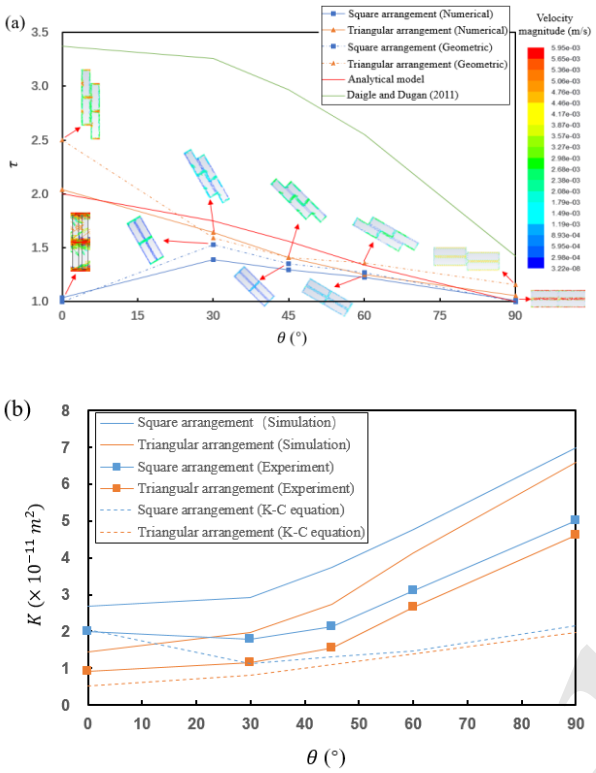

Figure 11. Effects of tilt angle on (a) tortuosity and (b) permeability

Based on the microfluidic chip's geometrical structure, we obtained a geometric solution for each microfluidic model (Fig. 11a). The geometric solutions were generally consistent with those determined by numerical simulation. However, the general observation was that results obtained by geometric solution were higher than those obtained by numerical simulation, especially for the triangular-arrangement model with a tilt angle of 0°. The geometric solution was 2.50, 25% higher than the numerical solution. The assumption of geometric analysis was that the streamline was a straight line in the center of the micro-channel, while the streamlines were curves in the numerical simulation, as shown in Fig. 11a. More details are given in Appendix C.

Due to the high aspect ratio, fabric in clay-rich sediments was reoriented during consolidation and shearing, causing a change in permeability. Daigle and Dugan (2011) developed a model to describe development of permeability anisotropy; it took into consideration the grain aspect ratio, porosity, and average angle of grains with respect to the horizontal plane. Results obtained by numerical simulation were compared to this model. It was clear that the model could not predict the numerical results accurately, because it produced far higher values than those acquired by numerical simulation. In the model, fabric particles were assumed to be flat cylindrical grains, while a 2D rectangular particle was idealized in this study. Thus, we propose an analytical model based on 2D rectangular particles (see Appendix D):

$$\tau = 1 + \frac{r^2\cos^2\theta}{(\frac{3\varepsilon}{1-\varepsilon}+2)(r\cos\theta+\sin\theta)} \tag{22}$$

where r is the aspect ratio. As shown in Fig. 12a, the results from the analytical model correspond to the numerical results.

Based on the results shown in Fig. 11a, we determined the effects of anisotropy on permeability by varying the tilt angle of unit cells (see Fig. 11b). Several general observations were obtained. At the same tilt angle, we observed lower permeability in the triangular-arrangement model than in the square-arrangement model, in both the numerical simulation and KC equation. With the same arrangement, permeability of microfluidic models increased by nearly four times as the tilt angle increased from 0° to 90°. Equivalent permeability of two-dimensional fractured rock-mass flow with different direction angles was discussed by Wang (2014). The same result: the equivalent permeability increased with the higher tilt angles, was obtained. Compared to the experimental permeability, numerical simulation led to higher permeability for the same model, while the KC equation led to lower permeability. The deviation was in two times. This indicated that the KC equation could roughly predict the permeability of the microfluidic test under the effects of anisotropy.

For the rectangular-micropillar model, the shape factor was the same. It was noted that the tortuosity was only 1.0389, yet the permeability was 2.03×10^{-11} m^2 for the square-arrangement model with a tilt angle of 0°. The effective porosity of this model was only 0.12, far lower than its intrinsic porosity of 0.41. The effective porosity is defined as the ratio of the pore volume with streamlines to the total volume. Due to the pore structure and wall effect of the microfluidic model with rectangular-micropillar arrangement, the phenomenon of preferential flow was clearly observed, as shown in Fig. 11a. Although

the pore channels were interconnected, the streamlines only exist in the pore channel of flow direction. Thus, compared to tortuosity, porosity had a more considerable influence on the permeability of porous media.

4.5 Effects of tortuosity on permeability

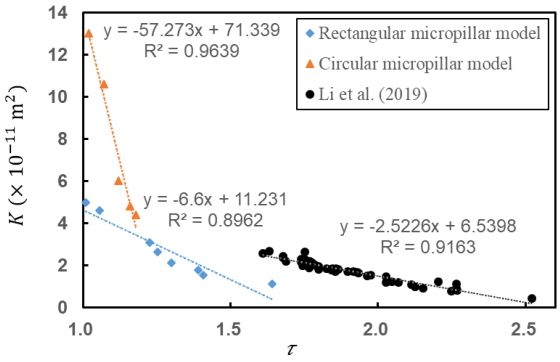

Figure 12. Variation of permeability with tortuosity

The effects of tortuosity on permeability in the experimental models are depicted in Fig. 12. As expected, there was an inverse relationship between the permeability and tortuosity. Permeability was found to decrease with an increase in tortuosity. The coefficient of determination R^2 for the rectangular-micropillar models and circular-micropillar models, as well as the results of Li *et al*. (2019), were 0.9639, 0.8962, and 0.9163, respectively. These values are all higher than 0.80, which means that the linear regression model fits the correlation between permeability and tortuosity. It is observed that the fitting coefficient for these three models were -57.237, -6.6, and -2.5226, respectively. Compared to the circular-micropillar models and the results of Li *et al*. (2019), permeability of the rectangular-micropillar models was the most sensitive to change in tortuosity. This is because the porosity increased from 0.33 to 0.90 for the rectangular-micropillar models, while the porosity for the circular-micropillar models was 0.41, and it was 0.30 for the models designed by Li *et al*. (2019). Compared to tortuosity, permeability is more sensitive to porosity.

When the porosity is constant, the permeability anisotropy ratio can be defined as the ratio of horizontal permeability to vertical permeability: $\delta = k_h/k_v$ (Daigle and Dugan, 2011). For the circular micropillar models and models of Li *et al*. (2019), the anisotropy ratio is defined as the ratio of maximum to minimum permeability. Therefore, the anisotropy ratio for the circular micropillar models is 5.43, while it is 3.28 for the models designed by Li *et al*. (2019). The latter were three-dimensional digital cores of tight sandstone. Overall, the higher the anisotropy ratio, the larger the change in permeability.

4.6 Effects of porosity on permeability

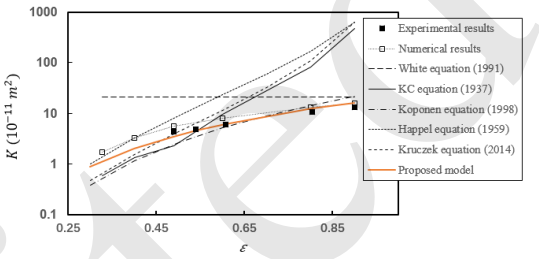

Figure 13. Comparison of permeability obtained from experiment and numerical simulations with that obtained from formulas available in the literature, for Asq-500

As a structural parameter, porosity plays a key role in permeability, especially when it is small. In the current work, the pores of microfluidic chip models were interconnected. In Fig.13, permeability generated by experiment and numerical simulation for Asq-500 are compared with permeability obtained from formulas available in the literature (Carman, 1939; Happel, 1959; White, 1991; Koponen *et al*., 1998; Kruczek, 2014). Details of these formulas are displayed in Table 3. Permeability generated by numerical simulation was consistent with that obtained from experiments, and the error was 9.78%~28.43%. The permeability prediction equations displayed in Table 3 are either the KC equation or modified KC equations, except the White equation (1991). For parallel plates duct flow, the equivalent permeability can be expressed by the White equation (1991). However, all the KC equations and modified KC equations fail to predict the permeability of microfluidic models accurately. For example, permeability estimated by the classic KC equation with the values of tortuosity in Fig. 8 roughly agreed with experimental results when the porosity was only in the range of 0.50-0.60. When the porosity was lower than 0.50, the permeability estimated by the KC equation was lower than the experimental results, and the error was within one time. When the porosity was

higher than 0.60, the permeability estimated by the KC equation was higher than the experimental results, and the error increased with the porosity increment. It was observed that the error was more than one order of magnitude. The Kozeny-Carman equation is not suitable for porosities above 60% (Koponen *et al*., 1998; Miguel 2012; Sharma et al., 2023). It was also observed that the Koponen equation (1998) had potential to predict the experimental results fairly accurately. Yet, it only fit the experimental points when porosity ranged from 0.60 to 0.80. When the porosity exceeded 0.80 or was below 0.60, the error was as high as 71%.

Table 3. Predicted equations of permeability in the literature

Authors	Models for permeability K
Carman (1939)	$K=\frac{1}{C_0\tau^2S^2}\frac{\varepsilon^3}{(1-\varepsilon)^2}$
Happel (1959)	$K=\frac{d^2}{32(1-\varepsilon)}[-\ln(1-\varepsilon)+\frac{(1-\varepsilon)^2-1}{(1-\varepsilon)^2+1}]$ Note: d is defined as the mean particle diameter
White (1991)	$K=\frac{h_0^2}{12}$ Note: h_0 is the height of the duct
Koponen et al., (1998)	$K=\frac{\varepsilon^3}{C_0{S_0}^2}$ Note: C_0 is 2 for cylindrical capillaries, S_0 is the ratio of fluid–solid interfacial area to total sample volume
Kruczek (2014)	$K=\frac{\Phi_s^2 d_p^2}{180}\frac{\varepsilon^3}{(1-\varepsilon)^2}$ Note: Φ_s is sphericity of the particles in the packed bed, d_p is the diameter of the equivalent spherical particle

When porosity was close to 1.0, the flow characteristics in the microfluidic chip model and the parallel plates duct flow model (White, 1991) were similar. This tendency is clear in Fig. 13. With a porosity of 1.0, the permeability obtained by White (1991) was 2.08×10^{-10} m^2, while that obtained by numerical simulation was 2.23×10^{-10} m^2. Based on above the analysis and literature research, a predicted model for the permeability of a microfluidic model was proposed:

$$K=\frac{1}{c\tau}\varepsilon^2 r_{cr}^2 \tag{23}$$

where r_{cr} is the pore radius and c is a shape parameter. For a quasi-2D microfluidic model, c is 3.4 (Mathavan and Viraraghavan, 1992). Carman (1956) proposed the hydraulic radius as a candidate for the pore radius, which is defined by the ratio of total pore volume to the total wetted surface area. The plot depicted in Fig.13 shows that the porosity is 0.60, and the permeability values obtained by the proposed model and experiment are 6.07×10^{-11} m^2 and 6.02×10^{-11} m^2, respectively. The permeability obtained by proposed model can be in line with the experimental results. In addition, permeability obtained by the proposed model is about 40% below the numerical results when the porosity is lower than 0.60. On the other hand, it matches the numerical results for high porosities, especially for a porosity of 0.90. In short, permeability of microfluidic models generated by the proposed model can predict the experimental and numerical results well compared to other equations in the literature.

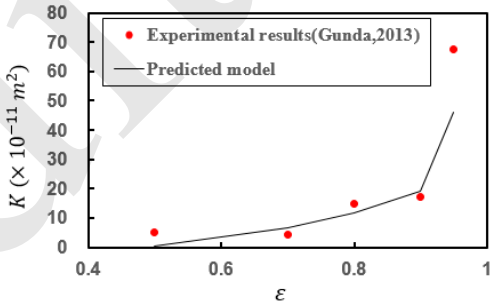

Figure 14. Comparison of experimental results (Gunda *et al*., 2013) with those producted by the predicted model

To validate the applicability of the predicted model, a comparison of experimental results obtained by Gunda *et al*. (2013) with the results of the predicted model is displayed in Fig. 14. In the experiments of Gunda *et al*. (2013), the micro-pillars were arranged in a square formation and the porosity of the microfluidic models ranged from 0.50 to 0.95. The predicted model appears to succeed in presenting the varying permeability of structured porous media.

4.7 Sources of error

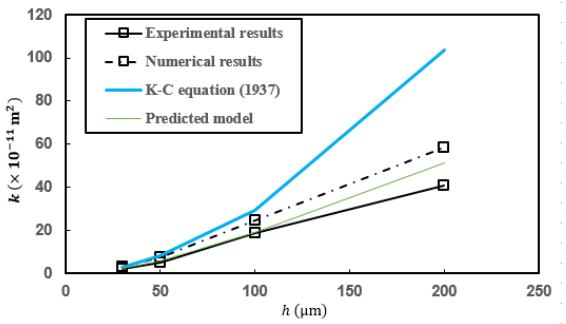

Figure 15. Comparison of experimental permeability with numerical simulation and different models ofAsq-0.60-500 plotted as a function of microchannel depth

Comparison of the experimentally derived permeability values with the numerical simulation and different models for Asq-0.60-500, was plotted as a function of microchannel depth (Fig. 15). Compared to experimental results, numerical simulation induced 25%~43% higher permeability values with the same microchannel depth, and the deviation increased proportionally to the channel depth increase. It was evident that microchannel depth was one important source of error. When the microchannel depth was 30 μm, both models could accurately predict the permeability of the microfluidic chips; but when the microchannel depth was larger than 50 μm, the KC equation failed to predict the permeability accurately. At the same time, when microchannel depth increased from 30 μm to 100 μm, the permeability generated by the predicted model was very consistent with the experimental data. When the microchannel depth was 200 μm, the permeability obtained by the predicted model was 51.17×10^{-11} m^2, while that obtained in the experiment was 40.86×10^{-11} m^2.

There was a limitation to the above permeability prediction models. In the KC equation, the Kozeny-Carman constant was affected by porosity, porous microstructure, tortuosity, and other factors. It was to be 5.0 for spherical particle porous based on generous experiments (Kaviany, 1995). For the peat bed, however, the Kozeny-Carman constant was 3.4 (Mathavan and Viraraghavan, 1992). For Asq-0.60-500, the tortuosity was about 1.2, so the Kozeny-Carman constant was 3.6. However, the Kozeny-Carman constant did not remain constant when the microchannel depth increased from 30 μm to 200 μm. Meanwhile, the specific surface area decreased from 0.111m^{-2} to 0.019 m^{-2} when the microchannel depth increased from 30 μm to 200 μm. The predicted model, it was meant to represent a quasi-two-dimensional porous medium with numerical simulation, and was applicable to microfluidic chip models. However, when the microchannel depth was 200 μm, the flow in microchannel pores was closer to three-dimensional conditions. Thus, there was error in the results. In addition, micropillars in the microfluidic models were fabricated in a uniform periodic arrangement. Yet, the type of packing and geometry of solid parts play the main relevant role on permeability (Koponen *et al*., 1997; Serrenho and Miguel, 2011; Koponen *et al*., 2017), and therefore warrant further study.

5 Conclusions

We estimated permeability for single-phase flow through microfluidic models with integrated micro-pillars, with Reynolds numbers varying between 0.83 and 142.98. The experimental results were compared with those obtained by numerical simulation and empirical theoretical models. The following conclusions can be drawn:

(1) Anisotropy induced by the tilt angle (0°~90°) of rectangular micropillars formed preferential flow and decreased the effective porosity. Especially for the square arrangement model with a tilt angle of 0°, the tortuosity was only 1.0389, yet the permeability was 2.03×10^{-11} m^2. The effective porosity of this model was only 0.12, far lower than its intrinsic porosity of 0.41. The Permeability of the various models increased by nearly four times as the tilt angle increased from 0° to 90°. When the tilt angle increases from 0° to 90°, the tortuosity declines from 2.04 to 1.03, causing the permeability to rise from 1.0×10^{-11} m^2 to 4.3×10^{-11} m^2. Therefore, an analytical tortuosity model based on the 2D rectangular particles is proposed.

(2) We observed that the threshold of the Reynolds number was 1. When *Re* is below the threshold, the permeability is independent of the Reynolds number. When *Re* is over this threshold, the viscous force plays a dominant role and the permeability drops as the Reynolds number increases.

(3) The permeability of the microfluidic chip

models is influenced by the diameter, arrangement, and shape of the micropillars. With the same porosity, due to the increase in side friction, microfluidic chips with smaller micropillar diameters yielded lower permeability than those with larger micropillar diameters; the permeability of triangular-arrangement model is 4.5%~7.4% lower than that of the square-arrangement model, due to a 5.1%~7.9% increase in tortuosity. Based on this, a mathematical model for calculating 2D circular-based soil tortuosity with different particle arrangements is proposed.

(4) The permeability generated by numerical simulation is consistent with that obtained from experiments, and the error is 9.78%~28.43%. However, permeability estimated by classic the KC equation roughly agrees with experimental results when the porosity is only 0.50-0.60. It was proved that the predicted model is suitable for estimate the experimental permeability of microfluidic models.

(5) As microchannel depth increases from 30 μm to 200 μm, the permeability obtained by numerical simulations is 25%~43% higher than that obtained by experiments. When the microchannel depth is more than 50 μm, the KC equation fails to predict the permeability of microfluidic chip models. The predicted model is therefore suitable for estimating experimental permeability with microchannel depths ranging from 30 μm to 200 μm.

Acknowledgments

This research was financially supported by the Basic Science Center Program for Multiphase Evolution in Hypergravity of the National Natural Science Foundation of China (Award No.: 51988101), the National Natural Science Foundation of China (Award No.: 42177118). Financial supports from the Chinese Program of Introducing Talents of Discipline to University (the 111 Project, B18047) is also acknowledged. The authors would also like to acknowledge the MOE Key Laboratory of Soft Soils and Geoenvironmental Engineering.

Author contributions

Shaokai Nie established the experiments, numerical simulation and wrote the first draft of the manuscript. Pengfei Liu, Kexin Chen, and Wenyuan Wang helped to analyze the results. Yunmin Chen provided important suggestions on the improvement of the study. Bate Bate revised and edited the final version.

Conflict of interest

Shaokai NIE, Pengfei LIU, Kexin CHEN, Wenyuan WANG, Yunmin CHEN and Bate BATE declare that they have no conflict of interest.

References

Akbari M, Sinton D, Bahrami M, 2009. Pressure drop in rectangular microchannels as compared with theory based on arbitrary cross section. *Journal of Fluids Engineering*, 131(4):0412021–0412028. https://doi.org/10.1115/1.3077143

Auset M, Keller AA, 2004. Pore-scale processes that control dispersion of colloids in saturated porous media. *Water Resources Research*, 40(3):1-11 https://doi.org/10.1029/2003WR002800

Bazylak A, Berejnov V, Markicevic B, et al., 2008. Numerical and microfluidic pore networks: towards designs for directed water transport in GDLs. *Electrochim Acta*, 53(26):7630–7637. https://doi.org/10.1016/j.electacta.2008.03.078

Bazarin RLM, De Lai FC, Naaktgeboren C, et al., 2021. Boundary Effects on the Tortuosity and Permeability of Idealized Porous Media, 136(3):743–764. https://doi.org/10.1007/s11242-020-01530-w

Bahrami M, Yovanovich MM, Culham JR, 2007. A novel solution for pressure drop in singly connected microchannels of arbitrary cross-section, *International Journal of Heat and Mass Transfer*, 50(14):2496-2502. https://doi.org/10.1016/j.ijheatmasstransfer.2006.12.019

Bate B, Chen C, Liu P, et al., 2022. The Migration and Deposition Behaviors of Montmorillonite and Kaolinite Particles in a Two-Dimensional Micromodel. *Materials*, 15(3):855. https://doi.org/10.3390/ma15030855

Cardona A, Santamarina JC, 2020. Carbonate rocks: Matrix permeability estimation. *AAPG Bulletin*, 103(1):131–144. https://doi.org/10.1306/05021917345

Chen C, Nie SK, Liu PF, 2021. Permeability characteristics of porous media base on 2D microfluidic chips. *Journal of Central South University (Science and Technology)*, 52(9):3295−3302. https://doi.org/10.11817/j.issn.1672-7207.2021.09.031

Cai JC, Hu XY, Standnes DC, et al., 2012. An analytical model for spontaneous imbibition in fractal porous media including gravity. *Colloids and Surfaces A: Physicochemical and Engineering Aspects.* 414:228–233. https://doi.org/10.1016/j.colsurfa.2012.08.047

Carman PC, 1939. Permeability of Saturated Sands, Soils and Clays. *Journal of Agricultural Science*, 29, 262-273. https://doi.org/10.1017/S0021859600051789

Carman PC, 1956. Flow of Gases through Porous Media, Elsevier, New York.

Collins RE, 1961. Flow of Fluids through Porous Materials. Reinhold Publishing Corporation, USA.

Conn CA, Ma K, Hirasaki HJ, et al., 2014. Visualizing oil displacement with foam in a microfluidic device with permeability contrast. *Lab Chip*, 14,3968–3977. https://doi.org/10.1039/C4LC00620H

Castillo-Araiza CO, Lopez-Isunzay F, 2008. Hydrodynamic

models for packed beds with low tube-to-particle diameter ratio. *International Journal of Chemical Reactor Engineering*, 6:1-14.
https://doi.org/10.2202/1542-6580.1550

Cao SC, Jung J, Radonjic M, 2019. Application of microfluidic pore models for flow, transport, and reaction in geological porous media: from a single test bed to multifunction real-time analysis tool. *Microsystem Technologies*, 25:4035-4052.
https://doi.org/10.1007/s00542-019-04612-y

Comiti J, Renaud MA, 1989. A new model for determining mean structure parameters of fixed beds from pressure drop measurements: Application to beds packed with parallelepipedal particles. *Chemical Engineering Science*, 44(7), 1539–1545.
https://doi.org/10.1016/0009-2509(89)80031-4

Chen C, 2021. Study on fine particle migration and permeability characteristics in porous media based on microfluidic chips. MS Thesis, Zhejiang University, China.

Chen K X, Liu P F, Wang W Y, et al., 2023. Effects of Capillary and Viscous Forces on Two-Phase Fluid Displacement in the Microfluidic Model. *Energy Fuels*, 37(22):17263–17276.
https://doi.org/10.1021/acs.energyfuels.3c03170

Daigle H, Dugan B, 2011. Permeability anisotropy and fabric development: A mechanistic explanation. Water Resources Research, 47, W12517.
https://doi.org/10.1029/2011WR011110

De S, Krishnan P, Schaaf J van der, Kuipers JAM, et al., 2018. Viscoelastic effects on residual oil distribution in flows through pillared microchannels. *Journal of Colloid and Interface Science*, Academic Press Inc. 510:262–271.
Https://doi.org/10.1016/j.jcis.2017.09.069

Dybbs A, Edwards RV, 1984. A new look at porous media fluid mechanics—Darcy to turbulent. Fundamentals of transport phenomena in porous media, J. Bear and M. Y. Corapcioglu, eds., Martinus Nijhoff, Dordrecht, The Netherlands, 199–256.
https://doi.org/10.1007/978-94-009-6175-3_4

Gunda NSK, Joseph J, Tamayol A, et al., 2013. Measurement of pressure drop and flow resistance in microchannels with integrated micropillars. *Microfluid Nanofluid*, 14:711–721.
https://doi.org/10.1007/s10404-012-1089-1

Happel J, 1959. Viscous flow relative to arrays of cylinders. *AIChE Journal*, 5(2):174–177.
https://doi.org/10.1002/aic.690050211

Hu R, Wan JM, Yang ZB, et al., 2018. wettability and flow rate impacts on immiscible displacement: a theoretical model. *Geophysical Research Letters*, 45:3077-3086.
https://doi.org/10.1002/2017GL076600

Huang YP, Yao F, Zhou B, et al., 2020. Numerical study on permeability characteristics of fractal porous media. *Chinese. Physics B*, 29(5):054701.
https://doi.org/10.1088/1674-1056/ab7b53

Kawagoe Y, Oshima T, Tomarikawa K, et al., 2016. A study on pressure-driven gas transport in porous media: from nanoscale to microscale. *Microfluidics and Nanofluidics*, 20(2).
https://doi.org/10.1007/s10404-016-1829-8

Kumar A, Reddy RG, 2003. Modeling of polymer electrolyte membrane fuel cell with metal foam in the flow-field of the bipolar/ end plates. *Journal of Power Sources*, 114(1):54–62.
https://doi.org/10.1016/S0378-7753(02)00540-2

Kosar A, Mishra C, Peles Y, 2005. Laminar flow across a bank of low aspect ratio micro pin fins. *Journal of Fluids Engineering*, 7(3):419–430.
https://doi.org/10.1115/1.1900139

Khabbazi AE, Hinebaugh J, Bazylak A, 2015. Analytical tortuosity–porosity correlations for Sierpinski carpet fractal geometries. *Chaos, Solitons & Fractals*,78:124–133.
https://doi.org/10.1016/j.chaos.2015.07.019

Kaviany M, 1995. Principles of Heat Transfer in Porous Media. *Mechanical Engineering Series*, Springer-Verlag, New York, Inc.

Koponen A, Kataja M, Timonen, J, 1996. Tortuous flow in porous media. *Physical Review E*, 54: 406–410.
https://doi.org/10.1103/PhysRevE.54.406

Koponen A, Kandhai D, Hellen E, et al., 1998. Permeability of Three-Dimensional Random Fiber Webs. *Physics Review Letters*, 80(4):716-719.
https://doi.org/10.1103/PhysRevLett.80.716

Koponen A, Kataja M, Timonen J, 1997. Permeability and effective porosity of porous media, *Physical Review E*, 56(3):3319-3325.
https://doi.org/10.1103/PhysRevE.56.3319

Koponen A, Ekman A, Mattila K, et al., 2017. The effect of void structure on the permeability of fibrous networks, *Transport in Porous Media*, 117(2):247-259.
https://doi.org/10.1007/s11242-017-0831-2

Kruczek B, 2014. Carman–Kozeny Equation. Springer Berlin Heidelberg.

Loosveldt H, Lafhaj Z, Skoczylas F, 2002. Experimental study of gas and liquid permeability of a mortar. *Cement and Concrete Research*, 32(9):1357-1363.
https://doi.org/10.1016/S0008-8846(02)00793-7

Lefebvre LP, Banhart J, Dunand DC, 2008. Porous metals and metallic foams: current status and recent developments. *Advanced Engineering Materials*, 10(9):775–787.
https://doi.org/10.1002/adem.200800241

Lu TJ, Stone HA, Ashby MF, 1998. Heat transfer in open-cell metal foams. *Acta Materialia*, 46(10):3619–3635.
https://doi.org/10.1016/S1359-6454(98)00031-7

Liu DD, Tran T, 2018. Microfluidic mixing using PDMS-based microporous structures. *Microfluidics and Nanofluidics*, 22:123.
https://doi.org/10.1007/s10404-018-2142-5

Lee SL, Yang JH, 1997. Modelling of Darcy–Forchheimer drag for fluid flow across a bank of circular pillars. *International Journal of Heat and Mass Transfer*,

40(13):3149–3155.
https://doi.org/10.1016/S0017-9310(96)00347-X

Lanfrey PY, Kuzeljevic ZV, Dudukovic MP, 2010. Tortuosity model for fixed beds randomly packed with identical particles. Chemical Engineering Science, 65:1891-1896.
https://doi.org/10.1016/j.ces.2009.11.011

Li T, Li M, Jing XQ, et al., 2019. Influence mechanism of pore-scale anisotropy and pore distribution heterogeneity on permeability of porous media. *Petroleum Exploration and Development*, 46(3):594–604.
https://doi.org/10.1016/S1876-3804(19)60039-X

Lock PA, Jing XD, Zimmerman RW, et al., 2012. Predicting the permeability of sandstone from image analysis of pore structure. *Journal of Applied Physics*, 92(10),6311-6319.
https://doi.org/10.1063/1.1516271

Mathavan GN, Viraghavan T, 1992. Coalescence filtration of an oil-in-water emulsion in a peat bed. *Water Research*, 1992, 26(1):91–98.
https://doi.org/10.1016/0043-1354(92)90116-L

Miguel AF, 2012. Non-Darcy Porous Media Flow in No-Slip and Slip Regimes, *Thermal Science*, 6(1):167-176.
https://doi.org/10.2298/TSCI100929001M

Nie SK, Liu PF, Ba T, et al., 2023. Seepage experiment and numerical simulation based on microfluidic chip model. *Journal of Zhejiang University (Engineering Science)*, 57(5):967-976.
https://doi.org/10.3785/j.issn.1008-973X.2023.05.013

Pozrikidis C, 1994. The motion of particles in the Hele-Shaw cell. *Journal of Fluid Mechanics*, 261:199-222.
https://doi.org/10.1017/S0022112094000315

Raeesi B, Piri M, 2009. The effects of wettability and trapping on relationships between interfacial area, capillary pressure and saturation in porous media: a pore-scale network modeling approach. Journal of Hydrology, 376(3-4):337–352.
https://doi.org/10.1016/j.jhydrol.2009.07.060

Straughan B, Harfash AJ, 2013. Instability in Poiseuille flow in a porous medium with slip boundary conditions. *Microfluid and Nanofluid*, 15(1):109–115.
https://doi.org/10.1007/s10404-012-1131-3

Selly S, Latief FDE, 2013. Tortuosity-porosity relationship in two-dimensional fractal model of porous media. *Fractals*, 21(2):1350013.
https://doi.org/10.1142/S0218348X13500138

Shen JT, Chen SY, 1989. The following behaviours of a spherical particle in fluid flow. Acta Aerodynamica Sinica, 7(1):50-58.

Serrenho A, Miguel AF, 2009. Simulation and Characterization of High Porosity Media for Aerosol Particle Processing, *Journal of Porous Media*, 12(12),1129-1137.
https://doi.org/10.1615/JPorMedia.v12.i12.10

Santamarina JC, Cho GC, 2004. Soil behavior: The role of particle shape. Proc. Skempton Conf., March, London.

Serrenho A, Miguel AF, 2011. Fluid flow and solid/fluid suspensions flow in 3-D packed beds of spheres: the effect of periodicity of fixed beds. *Defect and Diffusion Forum*, 312-315:871-876.
https://doi.org/10.4028/www.scientific.net/DDF.312-315.871

Sharma S, Geyer T, Arcondoulis EJG, 2023. On the influence of porous coating thickness and permeability on passive flow and noise control of cylinders. *Journal of Sound and Vibration*, 549:117563.
https://doi.org/10.1016/j.jsv.2023.117563

Tamayol A, Bahrami M, 2011a. In-plane gas permeability of proton exchange membrane fuel cell gas diffusion layers. *Journal Power Sources*, 196(7):3559–3564.
https://doi.org/10.1016/j.jpowsour.2010.11.109

Tamayol A, Bahrami M, 2011b. Transverse permeability of fibrous porous media. *Physical Review E*, 83(4):2.
https://doi.org/10.1103/PhysRevE.83.046314

Tamayol A, Bahrami M, 2011c. Water permeation through gas diffusion layers of proton exchange membrane fuel cells. *Journal Power Sources*, 196(15):6356–6361.
https://doi.org/10.1016/j.jpowsour.2011.02.069

Tamayol A, Khosla A, Gray B, et al., 2012. Creeping flow through ordered arrays of micro-pillars embedded in a rectangular minichannel. *International Journal of Heat and Mass Transfer*, 55(15–16): 3900–3908.
https://doi.org/10.1016/j.ijheatmasstransfer.2012.03.008

Tamayol A, Wong KW, Bahrami M, 2012. Effects of microstructure on flow properties of fibrous porous media at moderate Reynolds number. *Physical Review E*, 85:026318.
https://doi.org/10.1103/PhysRevE.85.026318

Tawfik H, Hung Y, Mahajan D, 2007. Metal bipolar plates for PEM fuel cell—a review. *Journal Power Sources*, 163(2):755–767.
https://doi.org/10.1016/j.jpowsour.2006.09.088

von Rickenbach J, Lucci F, Narayanan C, et al., 2014. Multi-scale modelling of mass transfer limited heterogeneous reactions in open cell foams. *International Journal of Heat and Mass Transfer*, 75:337–346.
https://doi.org/10.1016/j.ijheatmasstransfer.2014.03.060

White FM, 1991. Viscous Fluid Flow. New York: McGraw-Hill.
https://doi.org/10.1016/S0997-7546(00)01113-4

Wang P, 2014. Lattice Boltzmann Simulation of Permeability and Tortuosity for Flow through Dense Porous Media. *Mathematical Problems in Engineering*, 2014:166-183.
https://doi.org/10.1155/2014/694350

Wagner A, Eggenweiler E, Weinhardt F, et al., 2021. Permeability Estimation of Regular Porous Structures: A Benchmark for Comparison of Methods. Transport in Porous Media, 138,1–23.
https://doi.org/10.1007/s11242-021-01586-2

Wan J, Wilson JL, 1994. Colloid transport in unsaturated porous media. *Water Resources Research*, 30(4):857–864.
https://doi.org/10.1016/0148-9062(94)90237-2

Yang XH, Weldetsadik NT, Hayat Z, et al., 2019. Pressure drop of single phase flow in microchannels and its ap-

plication in characterizing the apparent rheological property of fluids. *Microfluidics and Nanofluidics*, 23:75. https://doi.org/10.1007/s10404-019-2241-y

Yazdchi K, Srivastava S, Luding S, 2011. Microstructural effects on the permeability of periodic fibrous porous media, *International Journal of Multiphase Flow*, 37(8):956–966. https://doi.org/10.1016/j.ijmultiphaseflow.2011.05.003

Yovanovich MM, 1974. A general expression for predicting conduction shape factors, AIAA, Thermophys. *Space Craft Control* 35:265–291. https://doi.org/10.2514/6.1973-121

Yang XH, Song SY, Yang C, et al., 2017. Permeability model of micro-metal foam with surface micro-roughness. *Microfluid and Nanofluid*, 21:32. https://doi.org/10.1007/s10404-017-1863-1

Yu BM, Li JH, 2004. A geometry model for tortuosity of flow path in porous media. *Chinese Physics Letters*, 21(8):1569–1571. https://doi.org/10.1088/0256-307X/21/8/044

Yang J, Yin ZY, Laouafa F, et al., 2019. Modeling coupled erosion and filtration of fine particles in granular Media. *Acta Geotechnica*, 14(6):1615-1627. https://doi.org/10.1007/s11440-019-00808-8

Yang J, Yin ZY, Laouafa F, et al., 2020a. Hydromechanical modeling of granular soils considering internal erosion. *Canadian Geotechnical Journal*, 57(2):157-172. https://doi.org/10.1139/cgj-2018-0653

Yang J, Yin ZY, Laouafa F, et al., 2020b. Three-dimensional hydromechanical modeling of internal erosion in dike-on-foundation. *International Journal for Numerical and Analytical Methods in Geomechanics*, 44(8):1200-1218. https://doi.org/10.1002/nag.3057

Yin ZY, Yang J, Laouafa F, et al., 2023. A framework for coupled hydro-mechanical continuous modelling of gap-graded granular soils subjected to suffusion. *European Journal of Environmental and Civil Engineering*, 27(8):2678-2699. https://doi.org/10.1080/19648189.2020.1795724

Zhang JF, 2011. Lattice Boltzmann method for microfluidics: models and applications. *Microfluid and Nanofluid*, 10(1):1–28. https://doi.org/10.1007/s10404-010-0624-1

Zhou C, Wang WY, Chen KX, et al., 2022. Influence of wettability in immiscible displacements with lattice Boltzmann method. *Journal of Zhejiang University-Science A (Applied Physics & Engineering)*, 23(9):704-720. https://doi.org/10.1631/jzus.A2200047